

Missing [CII] emission from early galaxies

S. Carniani¹*, A. Ferrara¹, R. Maiolino^{2,3}, M. Castellano⁴, S. Gallerani¹,
A. Fontana⁴, M. Kohandel¹, A. Lupi¹, A. Pallottini¹, L. Pentericci⁴,
L. Vallini⁵, and E. Vanzella⁶.

¹ *Scuola Normale Superiore, Piazza dei Cavalieri 7, I-56126 Pisa, Italy*

² *Institute of Astronomy, University of Cambridge, Madingley Road, Cambridge CB3 0HA, UK*

³ *Kavli Institute for Cosmology, University of Cambridge, Madingley Road, Cambridge CB3 0HA, UK*

⁴ *INAF - Osservatorio Astronomico di Roma, Via Frascati 33, I-00078 Monte Porzio Catone (RM), Italy*

⁵ *Leiden Observatory, Leiden University, PO Box 9500, 2300 RA Leiden, The Netherlands*

⁶ *INAF - Osservatorio di Astrofisica e Scienza dello Spazio, via Gobetti 93/3, 40129 Bologna, Italy*

Accepted XXX. Received YYY; in original form ZZZ

ABSTRACT

ALMA observations have revealed that [CII]158 μ m line emission in high- z galaxies is $\approx 2 - 3\times$ more extended than the UV continuum emission. Here we explore whether surface brightness dimming (SBD) of the [CII] line is responsible for the reported [CII] deficit, and the large $L_{\text{[OIII]}}/L_{\text{[CII]}}$ luminosity ratio measured in early galaxies. We first analyse archival ALMA images of nine $z > 6$ galaxies observed in both [CII] and [OIII]. After performing several uv -tapering experiments to optimize the identification of extended line emission, we detect [CII] emission in the whole sample, with an extent systematically larger than the [OIII] emission. Next, we use interferometric simulations to study the effect of SBD on the line luminosity estimate. About 40% of the extended [CII] component might be missed at an angular resolution of $0.8''$, implying that $L_{\text{[CII]}}$ is underestimated by a factor ≈ 2 in data at low (< 7) signal-to-noise ratio. By combining these results, we conclude that $L_{\text{[CII]}}$ of $z > 6$ galaxies lies, on average, slightly below the local $L_{\text{[CII]}} - \text{SFR}$ relation ($\Delta^{z=6-9} = -0.07 \pm 0.3$), but within the intrinsic dispersion of the relation. SBD correction also yields $L_{\text{[OIII]}}/L_{\text{[CII]}} < 10$, i.e. more in line with current hydrodynamical simulations.

Key words: galaxies: high-redshift - galaxies: evolution - galaxies: ISM - galaxies: formation

1 INTRODUCTION

In the last decade several deep multi-band imaging surveys have identified a large number of galaxies at early epochs. The emerging picture indicates that the cosmic period called Epoch of Reionization (EoR; $6 < z < 10$) is crucial in determining the assembly history of normal star-forming galaxies. Therefore, the characterisation of the interstellar medium (ISM) and star formation processes in galaxies at $z > 6$ is fundamental to understand the early phases of galaxy formation and evolution (Dayal & Ferrara 2018).

The advent of the Atacama Large Millimetre Array (ALMA) has enabled the first studies of the ISM in $z > 4$ “normal” star-forming galaxies with star-formation rates (SFRs) $< 100 \text{ M}_{\odot} \text{ yr}^{-1}$, comparable to those observed in low- z main-sequence galaxies (Ouchi et al. 2013; Ota et al. 2014; Maiolino et al. 2015; Capak et al. 2015; Knudsen et al. 2016; Inoue et al. 2016; Pentericci et al. 2016; Bradač et al. 2017; Matthee et al. 2017; Carniani et al. 2017, 2018b; Hashimoto et al. 2018; Matthee et al. 2019; Laporte et al. 2019; Harikane et al. 2020; Le Fèvre et al. 2019; Bakx et al. 2020). ALMA observations of rest-frame far-infrared (FIR) continuum emission and FIR fine-structure lines, such as [CII]($\lambda 158\mu\text{m}$) and [OIII]($\lambda 88\mu\text{m}$), can provide direct measurements of dust mass and temperature (e.g. Behrens et al. 2018; Bakx et al. 2020), molecular gas content (Zanella

et al. 2018; Pallottini et al. 2017a), metallicity (e.g. Vallini et al. 2015; Olsen et al. 2017), SFR (e.g. De Looze et al. 2014; Herrera-Camus et al. 2015; Carniani et al. 2018b; Schaerer et al. 2020), gas density, and ionisation parameter (Ferrara et al. 2019; Harikane et al. 2020).

The ALMA Large Program to INvestigate [CII] at Early times (ALPINE) survey has provided the first large sample of star-forming galaxies at $4 < z < 6$ (Le Fèvre et al. 2019). The sample includes 122 galaxies with $\text{SFR} > 10 \text{ M}_{\odot} \text{ yr}^{-1}$ and stellar mass $10^9 \text{ M}_{\odot} < M_{\star} < 10^{10.5} \text{ M}_{\odot}$. To optimise the detectability of diffuse emission, all galaxies have been observed in ALMA band 7 by adopting the most compact-array configurations (Bethertin et al. 2020) corresponding to angular resolutions $> 1''$ ($\approx 6.7 \text{ kpc}$ at $z = 4.5$). The [CII] line has been detected in 2/3 of the galaxies in the ALPINE survey and, by taking into account the upper limits from non-detections, Schaerer et al. (2020) have found that the [CII] luminosity ($L_{\text{[CII]}}$) scales linearly with SFR, in agreement with the relation observed in the local Universe (e.g. De Looze et al. 2014). This indicates no (or little) evolution of the $L_{\text{[CII]}} - \text{SFR}$ relation over the cosmic time up to $z \sim 6$.

At higher redshifts ($z > 6$), millimetre-interferometer observations have unveiled a more complex scenario. A large fraction ($\sim 50\%$) of the galaxy population observed in [CII] is characterized by a multi-component morphology (Matthee et al. 2017; Jones et al. 2017; Carniani et al. 2018a) showing spatial offsets between [CII] emission and the star-forming regions traced by rest-frame UV light (Matthee

* E-mail: stefano.carniani@sns.it

et al. 2017; Carniani et al. 2017, 2018b; Matthee et al. 2019). By taking into account such multi-component nature, some studies have shown that the $L_{\text{[CII]}}$ -SFR relation at early epochs seems to be fully consistent with the local relation (Matthee et al. 2017; Carniani et al. 2018a; Matthee et al. 2019), but its intrinsic scatter is two times larger than observed locally (Carniani et al. 2018b). Nevertheless, some studies have highlighted that galaxies with $SFR < 30 - 50 M_{\odot} \text{ yr}^{-1}$ and/or $z > 8$ are systematically below the local $L_{\text{[CII]}}$ -SFR relation (Pentericci et al. 2016; Knudsen et al. 2016; Bradač et al. 2017; Matthee et al. 2019; Laporte et al. 2019). Even taking into account a larger dispersion, some of these galaxies deviates from the relation more than 2σ . Such results may indicate that the $L_{\text{[CII]}}$ -SFR slope changes at low SFRs (Matthee et al. 2019), and/or that the relation itself evolves at $z > 6$ (Laporte et al. 2019).

Among $z > 6$ [CII] emitters observed with ALMA so far, nine UV-selected galaxies ($SFRs \lesssim 100 M_{\odot} \text{ yr}^{-1}$) and three submillimeter galaxies ($SFRs \gtrsim 300 M_{\odot} \text{ yr}^{-1}$) have been observed in [OIII] as well (Inoue et al. 2016; Carniani et al. 2017; Laporte et al. 2017; Walter et al. 2018; Marrone et al. 2018; Tamura et al. 2019; Hashimoto et al. 2019; Harikane et al. 2020). The [OIII] line has been detected in all galaxies and the reported [OIII]/[CII] luminosity ratios spans a range between 1 and 20, which is systematically higher than the average line ratio observed in local star-burst and metal-poor dwarf galaxies (Harikane et al. 2020). The observed [OIII]/[CII] ratios are also in tension with most of current cosmological and zoom-in simulations, which struggles to predict FIR luminosity ratios > 2 (Pallottini et al. 2017b; Olsen et al. 2017; Katz et al. 2017, 2019; Lupi & Bovino 2020). On the other hand, cosmological hydrodynamic simulations by Arata et al. (2020) have suggested that high [OIII]/[CII] luminosity ratios, more in line with ALMA observations, can occur during starburst phases.

The origin of the relatively low (high) [CII] ([OIII]) luminosities reported in $z > 6$ normal¹ star-forming galaxies is still debated. Several studies have speculated on different explanations to reproduce current interferometric observations. Vallini et al. (2015) find that the [CII] luminosity decreases with decreasing gas metallicity and, therefore, the [CII] deficit may indicate that these galaxies are very metal-poor systems. However, recent simulations and theoretical models have shown that gas metallicity, unless very low (e.g. $Z < 0.1 Z_{\odot}$), plays a sub-dominant role in shaping the [CII]-SFR relation (Ferrara et al. 2019; Pallottini et al. 2019; Lupi & Bovino 2020). Upward deviations with respect to the Kennicutt-Schmidt relation due to a starburst phase, could strongly depress [CII] emission. This is because the associated strong interstellar radiation field depletes the C^{+} ion abundance by turning C into higher ionization states (Ferrara et al. 2019). For the same reason, the abundance of [OIII] in the ionized layer is enhanced. The combination of the two effects boosts the [OIII]/[CII] luminosity ratio (Harikane et al. 2020; Arata et al. 2020). The low [CII] emission could also be associated to a low (0-10%) PDR covering fraction due to the compact size of high- z galaxies or galactic outflows (Harikane et al. 2020). The latter scenario seems to be also supported by recent observational evidences revealing outflowing gas in star-forming galaxies at $z = 4 - 6$ (Gallerani et al. 2018; Fujimoto et al. 2019; Sugahara et al. 2019; Ginolfi et al. 2020b). Finally, Kohandel et al. (2019) discuss that the line width of the FIR line, and thus disc inclination, may be responsible of the non-detections. In fact, at a fixed line luminosity and spectral resolution, narrower emission lines

easily push the peak flux above the detection limit with respect to broader lines. If the [OIII] and [CII] had different line profile, the FIR line with narrower line width would be easily detectable.

Another possible scenario for the [CII] deficit is that current FIR luminosity measurements suffer from flux losses due the spatially-extended emission of the carbon line. For example Carniani et al. (2017) show that about 70% of the diffuse [CII] emission of BDF-3299, a star-forming galaxy at $z = 7$, is missed in ALMA observations with angular resolution (θ_{beam}) of $0.3''$, while the total emission is recovered in the datasets with $\theta_{\text{beam}} = 0.6''$. Another similar case is Himiko, a Ly α emitter at $z \sim 6$. The flux losses due to the surface brightness dimming led to a non-detection of the FIR line in first ALMA project. The line was detected successively in a later ALMA program with similar sensitivity but lower angular-resolution (Ouchi et al. 2013; Carniani et al. 2018a). It is therefore fundamental to quantify the effect of angular resolution on the FIR line luminosity measurements in order to investigate in details the [CII]-SFR relation and the [OIII]/[CII] relation in the EoR.

Here we thus focus on the spatial extension of the FIR lines and the impact of surface brightness dimming (SBD) on the line detection and flux measurements at $z > 6$. We re-analyse the ALMA data of all those UV-selected $z = 6 - 9$ star-forming galaxies observed in [CII] and [OIII] in order to verify the robustness of some [CII] non-detection and compare the extent of the two FIR emission lines. We then compare the observations with simulations to verify whether or not the [CII] luminosity could be underestimated because the line flux is spatially resolved out. Finally we investigate the $L_{\text{[CII]}}$ -SFR and $L_{\text{[OIII]}}/L_{\text{[CII]}}$ line ratios at $z > 6$ by taking into account the SBD effect. The paper is organised as follows. ALMA observations and data reduction are presented in Sec. 2, while their analysis is discussed in Sec. 3. In Sec. 4, we discuss mock ALMA observations in order to investigate the dependence of luminosity measurements² on both angular resolution and sensitivity; we also compare the simulations with real data to assess our results. We then discuss the implications on the $L_{\text{[CII]}}$ -SFR relation and [OIII]/[CII] luminosity ratio in Sec.s 5.1 and 5.2, respectively. Finally, we summarise and draw our conclusions in Sec. 6.

2 OBSERVATIONS AND DATA ANALYSIS

We have retrieved ALMA archival data³ for galaxies in the literature that have been observed in both [CII] and [OIII]. The list of the sources is shown in Table 1.

The observations have been calibrated with the pipeline script delivered with the raw data from the archive, and by using the Common Astronomy Software Applications package (CASA; McMullin et al. 2007). We have used the appropriate package version for each target, as indicated in the pipeline scripts. The final datacube for each target has been generated with the `tclean` task by selecting a pixel scale as large as 1/5 of the ALMA beam. We have used a natural weighting that returns the best surface brightness sensitivity. We have not performed any spectral rebinning, i.e. preserving the

² We adopt the cosmological parameters from Planck Collaboration et al. (2015): $H_0 = 67.7 \text{ km s}^{-1} \text{ Mpc}^{-1}$, $\Omega_m = 0.308$ and $\Omega_{\Lambda} = 0.70$, according to which $1''$ at $z = 6$ corresponds to a proper distance of 5.84 kpc. SFR estimates have been calculated by using the relations reported in Kennicutt & Evans (2012), assuming a Kroupa (2001) IMF.

³ We note that for SXDF-NB1006-2 and BDF-3299 we use additional public datasets (2016.A.00018.S and 2016.1.00856.S) that were not included in previous studies (Inoue et al. 2016; Carniani et al. 2017).

¹ galaxies with $SFR \lesssim 100 M_{\odot} \text{ yr}^{-1}$ that represent the bulk of galaxy population.

original spectral resolution of the raw data. The sensitivities of the final cubes (Table A1) are consistent with those reported by previous works. For the non-detections, we have also produced cubes with lower angular resolution by performing different uv -tapering, from $0.2''$ to $2''$. As explained in Sec. 3, decreasing the angular resolution of the final images is crucial to detect faint, extended emission. The uv -tapering procedure has enabled us to detect the [CII] line in those galaxies in which previous works quoted a non-detection.

We have constructed the [CII] flux map with the CASA task `immoments` by integrating the channels of the line in the final datacube. The integrated flux density has been estimated from the region that encompasses the 2σ contours around the peak in the flux map. In those galaxies where the area of the 2σ -contour region is smaller than $2\times$ ALMA-beam area, we measure the integrated flux density from a circular aperture with diameter as large as $1.5\times$ the major-axis of the ALMA beam and centred at the emission peak of the flux map. We have then calculated the uncertainty on the flux density rescaling the noise by the square root of the number of independent beams in the selected region.

We have also estimated the extent of the FIR line emission by performing a 2D-Gaussian fitting of the [CII] flux map with the CASA task `imfit`. In addition to the image plane analysis, we have also performed the size measurements on the uv plane by collapsing the spectral channels around the line peak and following the procedure explained in (Carniani et al. 2019), which adopts the GALARIO package by Tazzari et al. (2018). The two measurements are in agreement within the errors.

ALMA observations properties and all measurements are reported in Tables 1 and A1. For those galaxies in which our results are consistent with those reported in previous studies we list the measurements of the primary works. In particular, the results of our analysis differ from previous works only in some [CII] data, as discussed in Sec. 3.

In the paper we have also used rest-frame UV images from Hubble Space Telescope (*HST*) and UK Infrared Telescope (UKIRT) images to compare the location of the [CII] emission with that of the UV region. The relative astrometry of ALMA and *HST* images have been calibrated by matching ALMA calibrator and foreground sources (if any) to the GAIA Data Release 1 catalogue (Gaia Collaboration et al. 2016).

3 INDIVIDUAL TARGETS: RESULTS

In this Section, we present the results from our ALMA data analysis for the individual targets listed in Table 1, along with a comparison with previous findings in the literature.

3.1 SXDF-NB1006-2, A2744-YD4, and MACSJJ149-JD1

We focus initially on SXDF-NB1006-2 and the two lensed galaxies A2744-YD4 and MACSJJ149-JD1. In these sources, previous studies have detected the [OIII] line but reported a non-detection for [CII] (Inoue et al. 2016; Laporte et al. 2019). These galaxies seem to be characterised by a high FIR line ratio ($L_{[\text{OIII}]} / L_{[\text{CII}]} > 10$ for SXDF-NB1006-2 and MACSJJ149-JD1, and $L_{[\text{OIII}]} / L_{[\text{CII}]} > 3$ for A2744-YD4) that is a few times higher than those observed in the local Universe (De Looze et al. 2014; Cormier et al. 2015; Harikane et al. 2020) and simulations (Pallottini et al. 2019; Arata et al. 2020).

Given the results of previous studies, we have changed the data reduction method to verify if the [CII] non-detection is due to resolving out of the line emission. We have thus generated 10 different

ALMA cubes for each target by varying the uv -taper parameter⁴ from $0.2''$ to $2''$ in steps of $0.2''$. We stress that the uv -tapering decreases both angular resolution and sensitivity of the final images. Therefore our approach of analysing images of the same target with different uv -tapering and, hence, ALMA beams, enables us to find the best sensitivity-angular resolution combination that optimises the detection of extended emission. In each cube, we have then performed a blind-line search within $5''$ from the location of the targets and from -1000 km s^{-1} to 1000 km s^{-1} with respect to the [OIII] redshift (see App. B for details). Finally, we have selected only those detections with a level of confidence⁵ $> 3.6\sigma$, and among this final sample we have extracted the line candidate with the highest confidence level.

In all three galaxies we have found a candidate line with a significance level $> 3.8\sigma$ in the integrated uv -tapered map at the redshift of either [OIII] or Ly α line. In Fig. 1 we show the results of our blind line search procedure. Luminosity estimates are reported in Table 1 while other measurements are listed in App. A1. The [CII] detection for both SXDF-NB1006-2 and MACSJJ149-JD1 is co-spatial with the UV emission, while the [CII] emission in A2744-YD4 is located $0.8''$ away from the galaxy.

Given the large ALMA beam used, the spatial offset of A2744-YD4 might be consistent with the astrometric accuracy of ALMA⁶, σ_p , given by

$$\sigma_p = 60 \text{ mas} \left(\frac{100 \text{ GHz}}{\nu_{\text{obs}}} \right) \left(\frac{10 \text{ km}}{b} \right) \left(\frac{1}{\text{SNR}} \right), \quad (1)$$

where ν_{obs} is the observing frequency, b is the maximum baseline, and SNR is the signal-to-noise ratio of the source peak. The astrometric uncertainty for A2744-YD4 ALMA observations is expected to be $\sim 0.6''$. Therefore the location of the [CII] and UV regions are consistent within $1.3\sigma_p$. However, we also note that Laporte et al. (2019) report a spatial offset between the [OIII] and dust continuum emission as well. The situation of A2744-YD4 could thus resemble what observed in BDF-3299, where the [CII], [OIII], and UV emission are tracing different components of the same system with different properties (Carniani et al. 2017). The spatial offsets could also be associated to either material ejected by galactic outflows or a galaxy merger (Maiolino et al. 2015; Vallini et al. 2015; Pallottini et al. 2017a; Katz et al. 2017; Gallerani et al. 2018; Kohandel et al. 2019). The merger scenario seems to be supported by the fact that the UV images show other group members around A2744-YD4 (Zheng et al. 2014).

3.2 BDF-3299

Maiolino et al. (2015) and Carniani et al. (2017) present Cycle-1 and -2 ALMA observations of BDF-3299, a Ly α -emitting galaxy at $z = 7.1$ (Vanzella et al. 2011; Castellano et al. 2016). ALMA images have revealed a [CII] emission consistent with the Ly α redshift but spatially offset by $0.7''$ to the optical (UV-rest frame) emission. By using serendipitous sources found in the ALMA field-of-view, the authors conclude that the displacement is not ascribed to astrometric uncertainties.

In Cycle 4, we were awarded ALMA time to obtain deeper

⁴ The uv -tapering procedure reduces the angular resolution by scaling down the weight of the uv -data from the longer baselines. It thus smooths the final image but at the expense of sensitivity since part of the data are excluded or data usage is non-optimal.

⁵ We adopt the detection threshold used in the ALPINE survey (Bethérmin et al. 2020).

⁶ Sec. 10 of the ALMA technical handbook

Table 1. List of targets observed with ALMA in [CII] and [OIII], and their FIR line luminosities. All estimates are corrected for magnification.

Target (1)	z (2)	$L_{[\text{CII}]} [10^8 L_\odot]$ (3)	$L_{[\text{OIII}]} [10^8 L_\odot]$ (4)	$L_{[\text{OIII}]} / L_{[\text{CII}]}$ (5)	$(L_{[\text{OIII}]} / L_{[\text{CII}]})^{\text{corr}}$ (6)
MACSJ1149-JD1	9.11	$0.12 \pm 0.03^{*a} (< 0.04)^\dagger$	0.74 ± 0.16^b	6.2 ± 2.0	4.2 ± 1.4
A2744-YD4	8.38	$0.18 \pm 0.06^{*a} (< 0.2)^\dagger$	0.70 ± 0.17^c	3.9 ± 1.6	3.2 ± 1.3
MACSJ0416-Y1	8.31	$1.4 \pm 0.2^{*d}$	12 ± 3^e	9 ± 2	8 ± 2
SXDF-NB1006-2	7.21	$1.7 \pm 0.4^a (< 0.8)^\dagger$	9.8 ± 2.2^f	5.8 ± 1.9	4.3 ± 1.4
B14-65666	7.16	11.0 ± 1.4^g	34 ± 4^g	3.1 ± 0.5	2.8 ± 0.5
BDF-3329	7.11	0.67 ± 0.09^a	1.8 ± 0.2^i	2.7 ± 0.5	1.8 ± 0.5
J0217	6.20	14 ± 2^j	85 ± 2^j	6.1 ± 0.9	5.7 ± 0.9
J0235	6.09	4.3 ± 0.7^j	38 ± 3^j	8.8 ± 1.6	7.8 ± 1.4
J1211	6.03	14 ± 1^j	48 ± 7^j	3.4 ± 0.6	3.4 ± 0.6

Columns. (1) Name of the target. (2) redshift. (3,4) Observed [CII] and [OIII] luminosities. (5) [OIII]-to-[CII] luminosity ratio. (6) [OIII]-to-[CII] luminosity ratio corrected for the SBD effect (see text). **Notes.** * Lensed galaxies. We assume a magnification factor $\mu = 10, 2$, and 1.4 for MACSJ1149-JD1, A2744-YD4, and MACSJ0416-Y1, respectively. † previous upper limits by Inoue et al. (2016) and Laporte et al. (2019). **References:** ^a this work; ^b Hashimoto et al. (2019); ^c Laporte et al. (2017); ^d Bakx et al. (2020); ^e Tamura et al. (2019); ^f Inoue et al. (2016); ^g Hashimoto et al. (2019); ^h Maiolino et al. (2015); ⁱ Carniani et al. (2017); ^j Harikane et al. (2020).

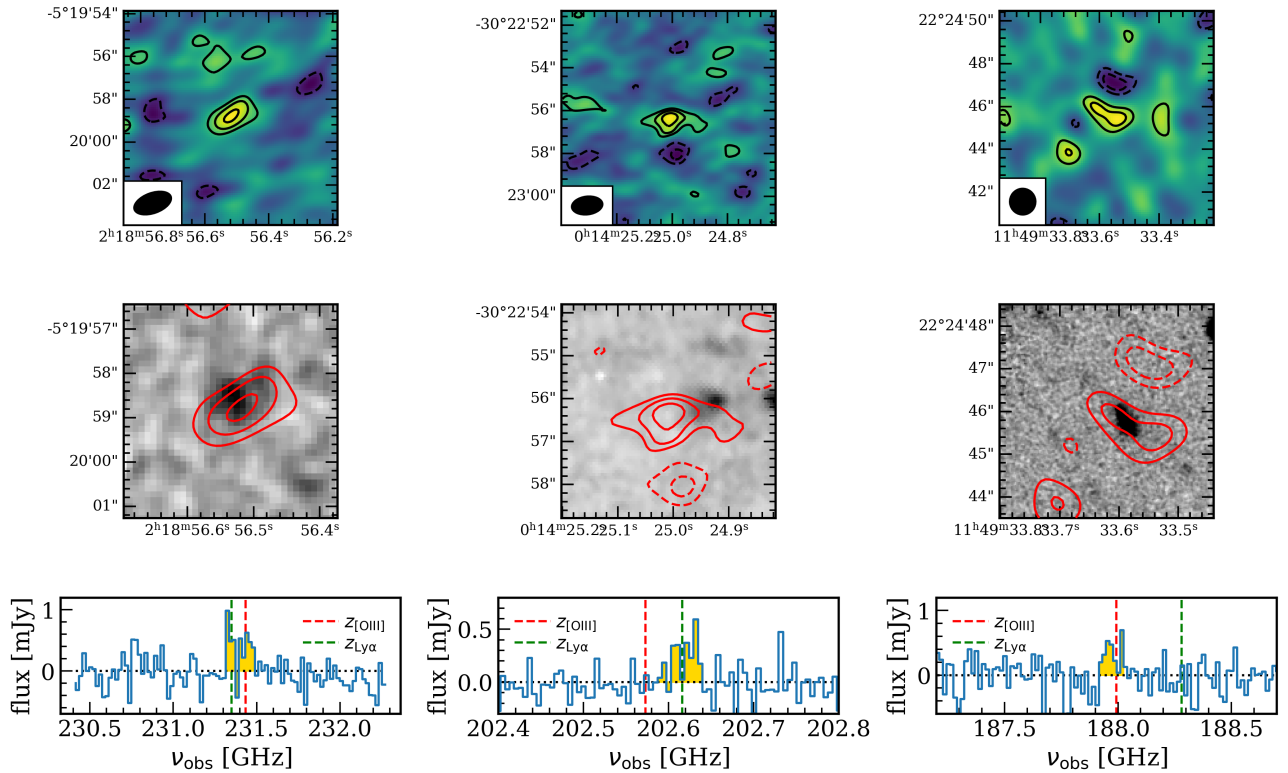


Figure 1. From left to right panels: [CII] line detections of SXDF-NB1006-2, A2744-YD4, and MACSJ1149-JD1. In the top row we report the [CII] maps obtained by collapsing the ALMA datacube over the line width of the detected line. Contours are at level of $\pm 2, 3$, and 4σ . Middle row illustrates zoom-in maps of rest-frame UV emission and the red contours are the [CII] emission. The bottom row shows the [CII] spectra extracted from the 2σ -contour regions. The [OIII] and $\text{Ly}\alpha$ redshifts are highlighted with vertical red and green dashed lines, respectively.

[CII] observations of BDF-3299 with respect to those presented by Maiolino et al. (2015). The proposed observations aimed at detecting extended emission around the galaxy, but only 25% of the proposed program was completed. The achieved sensitivity, $\sigma_{20\text{km/s}}^7 = 120 \mu\text{Jy beam}^{-1}$, is comparable to that of previous observations (Maiolino et al. 2015; Carniani et al. 2017). The program was carried

out with a semi-compact array configuration resulting in an angular resolution of $0.6'' \times 0.5''$.

In the new dataset we have detected the [CII] line with a level of significance of 5σ and spatially offset by $\sim 0.7''$ (~ 3.7 kpc) from the UV emission (Fig. 2). In this case the spatial offset is 3.5 times larger than the $\sigma_p = 0.2''$ and is unlikely to be related to the astrometric calibration of ALMA dataset. Both redshift and line width are consistent with the [CII] properties estimated by Maiolino

⁷ Sensitivity level in spectral bins of 20 km s^{-1}

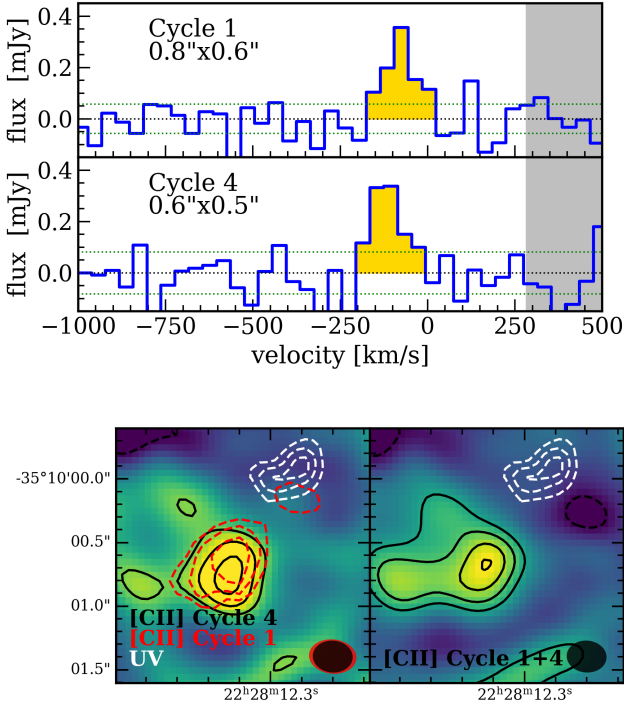


Figure 2. *Top:* [CII] spectra of BDF-3299 from the old (Cycle 1) and new (Cycle 4) ALMA programs, extracted at the location of [CII] clump. *Bottom:* Left panel shows the [CII] map of BDF-3299 produced only from the new Cycle-4 dataset; the right panel illustrates the flux map from the combined dataset (Cycle 1 + Cycle 4). The black contours show ± 2 , ± 3 , ± 4 , and $\pm 5\sigma$. Red dashed contours trace the Cycle-1 [CII] map reported by [Maiolino et al. \(2015\)](#) and contours are at levels 2, 3 and 4 times noise per beam, while white dashed contours correspond to the rest-frame UV emission from *HST* observations ([Castellano et al. 2016](#)). We report the synthesised ALMA beam in the bottom-right corners.

[et al. \(2015\)](#) and [Carniani et al. \(2017\)](#). This new independent dataset confirms the robustness of the displaced [CII] detection.

By combining the new and old datasets we have reached a sensitivity of $\sigma_{\text{cont}} = 8 \mu\text{Jy beam}^{-1}$ and $\sigma_{20\text{km/s}} = 90 \mu\text{Jy beam}^{-1}$ in the continuum and line map, respectively. Despite the deeper images, we have detected neither the continuum nor [CII] emission at the location of the UV region.

The bottom panel of Fig. 2 shows the flux map of the spatially offset [CII] emission obtained from the combined dataset. The peak of the emission has a significance level of 5.2σ and the total integrated flux is $S\Delta\nu = 52 \pm 7 \text{ mJy km s}^{-1}$, which is consistent within the error with previous measurements. We thus infer a [CII] luminosity of $(6.7 \pm 0.9) \times 10^7 L_{\odot}$.

In the new map we notice that the displaced [CII] emission is more extended with respect to what observed in previous shallower observations. The [CII] morphology of the map can be described by two components, dubbed A and B in Fig. 3. The spectra extracted from the individual regions indicate that the two [CII] components have similar redshifts but different line widths ($FWHM_A = 143 \text{ km s}^{-1}$ and $FWHM_B = 80 \text{ km s}^{-1}$).

We conjecture that the extended emission toward East represents an additional fainter and smaller satellite member of BDF-3299 system. A similar scenario is in agreement with zoom-in simulations ([Pallottini et al. 2019](#)), predicting that high- z systems are surrounded

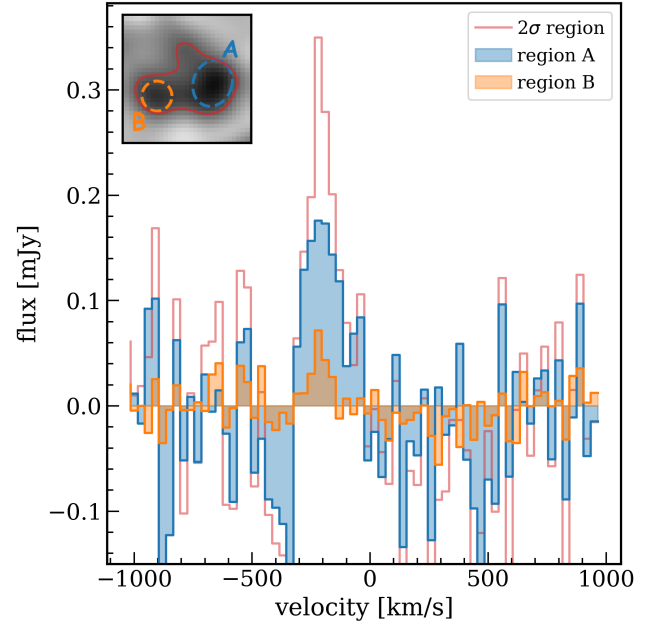


Figure 3. [CII] spectra of BDF-3299 obtained from the combined ALMA dataset. Red line shows the spectrum of the total [CII] emission arising from the 2σ -contour region (red contour in the inset). The spectra of the individual [CII] components, A and B, are shown in blue and orange. The top-left inset illustrates the apertures adopted to extract the spectra of the two [CII] components.

by satellites with $\text{SFR} < 5 M_{\odot} \text{ yr}^{-1}$. These satellites are located within 100 kpc from the main galaxy, and are too faint to be detected in shallow UV images. However, such satellites could be visible in either deep [CII] observations as BDF-3299 or rest-frame UV *HST* observations of strongly lensed systems ([Vanzella et al. 2017, 2019](#)).

Another possibility is that the extended [CII] emission is tracing metal-enriched circumgalactic medium (CGM) around BDF-3299. Recent high- z observations have indeed shown that galactic outflows ([Gallerani et al. 2018](#); [Fujimoto et al. 2019](#); [Ginolfi et al. 2020b](#)) and gas stripping by tidal interactions ([Ginolfi et al. 2020a](#)) might be responsible of the carbon enrichment on kiloparsec scales. The [CII] emission on large scale is then excited by the UV radiation of the galaxy ([Carniani et al. 2017](#)). However in this case one would expect to observe a gradient of velocity between the two [CII] components associated to either outflowing or inflowing kinematics as observed in other high- z systems (e.g. [Jones et al. 2017](#); [Ginolfi et al. 2020a](#)). However, distinguishing between satellites or CGM requires either more sensitive [CII] images or JWST observations enabling us to identify the emission (if any) of the stellar population from each individual component.

3.3 MACSJ0416-Y1, B14-65666, J0235, J1211, and J0217

For the remaining systems (MACSJ0416-Y1, B14-65666, J0235, J1211, and J0217) for which co-spatial [CII] and [OIII] emissions have been already reported in the literature ([Tamura et al. 2019](#); [Hashimoto et al. 2019](#); [Harikane et al. 2020](#); [Bakx et al. 2020](#)), we have found results consistent with previous works. In Table 1 we list the [CII] and [OIII] luminosities.

Since for these galaxies the two FIR lines have been detected with high signal-to-noise ratio ($\text{SNR} > 8$), we take advantage of these

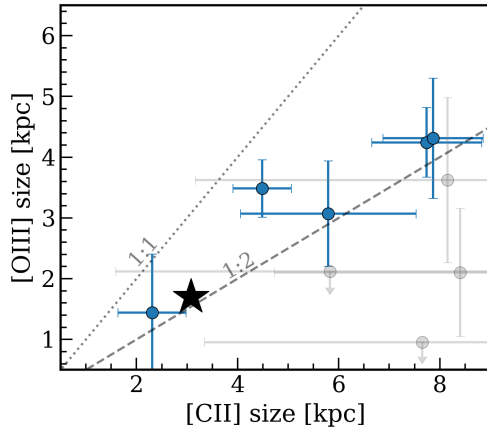


Figure 4. Comparison between [OIII] and [CII] emission extension of our sample. The circle blue marks indicate the size measurements of MACSJ0416-Y1, B14-65666, J0235, J1211, and J0217, which are detected with high SNR. The grey circles show the extents of the remaining galaxies identified with a lower SNR (MACSJ1149-JD1, A2744-YD4, SXDF-NB1006-2, and BDF-3299). The star symbol represents the [OIII] and [CII] sizes of Freesia, the most massive galaxy in the Pallottini et al. (2019) simulations. The dotted and dashed lines indicate 1:1 and 1:2 relation, respectively.

observations to investigate the extent of the FIR lines, as shown in Fig. 4 (and Table A1). We notice that [CII] is systematically larger than the [OIII] and its extent is about two times larger than that of oxygen line. This is consistent with recent simulations by Pallottini et al. (2019) where the [OIII] is concentrated in a compact region of 0.85 kpc, while the [CII] arise from a more extended area with a radius of 1.54 kpc. Simulations and observations suggest that distinct FIR emission lines trace different regions of the same galaxy, characterised by different metallicity or excitation (ionisation parameter) properties (Carniani et al. 2017; Katz et al. 2017; Pallottini et al. 2019).

As we will discuss in Sec. 5 there are various scenarios to explain the extended component of the [CII] line. Here we note that the different extent of [CII] and [OIII] emission could dramatically affect the measured [OIII]/[CII] ratios. Indeed, while in images with an intermediate ALMA spatial-resolutions (i.e. $\sim 4 - 5$ kpc) the [OIII] emission may appear as point-like, [CII] emission could be spatially resolved and a fraction of the extended emission could be missed due to the low sensitivity. In the next Section we make use of ALMA simulations to quantify this effect in available observations.

4 [CII] SURFACE BRIGHTNESS DIMMING

We have performed ALMA simulations with different array configurations to estimate how the angular resolution affects the [CII] and [OIII] flux measurements. This enables us to assess whether a fraction of the [CII] emission might be missed when the FIR line flux is spatially resolved and the sensitivity is too low to recover the total surface brightness.

4.1 Simulations

We have used the `simobserve` task of CASA to produce mock interferometric observations of galaxies at $z \sim 7$. As source models,

we have used a 2D Gaussian profile for the [CII] and [OIII] surface brightness with major-axes⁸ (D_{source}) fixed to $0.8''$ (≈ 4.6 kpc) and $0.45''$ (≈ 2.6 kpc), respectively for the two FIR lines. The assumptions on the D_{source} are based on current ALMA observations (see Fig. 4 and Carniani et al. 2018b). We have then assigned to each source a random axis ratio ($0.1 < b/a < 1.0$) and position angle.

For simplicity, we have assumed $L_{\text{[CII]}} = L_{\text{[OIII]}} = 5 \times 10^8 L_{\odot}$ for all mock sources. We have thus set the integrated flux density to $0.43 \text{ Jy km s}^{-1}$ for the [CII] sources and $0.21 \text{ Jy km s}^{-1}$ for the [OIII] mock targets, and assumed a line width of 200 km s^{-1} . Once fixed the line properties, we have generated two set of simulations.

For the first set of simulations we have computed 100 synthetic observations for each of the five most compact array configurations at the observed line frequencies of 230 GHz and 410 GHz, which correspond to the redshifted frequencies of the two FIR lines for a galaxy at $z \sim 7$. The on-source exposure time (t_{exp}) of each line has been fixed for all simulations in order to obtain the same noise level per ALMA beam independently of array configurations. By using the ALMA exposure time calculator (ETC), we have estimated $t_{\text{exp}} = 16$ minutes for the [CII] pointings and $t_{\text{exp}} = 6.5$ hours for the [OIII] pointings. Such t_{exp} enable the detection of the two FIR lines with a level of significance of $\sim 10\sigma$ if the target is a point-like source.

In the second set of mock interferometric data we have run several simulations for each array configuration with different t_{exp} . The emission in the final images has hence different SNR depending both on the ALMA beam ($0.4'' < \theta_{\text{beam}} < 2''$) and sensitivity ($5 \text{ mJy km s}^{-1} \text{ beam}^{-1} < \sigma < 140 \text{ mJy km s}^{-1} \text{ beam}^{-1}$). These mock data have allowed us to investigate the impact of the noise level on the detection of extended emission.

In the resulting mock images of both sets of simulations we have finally measured the FIR line fluxes by adopting the same procedure used in real images and described in Sec 2.

4.2 Analysis of mock data

4.2.1 Simulations with fixed exposure times

Let us consider first the set of ALMA simulations obtained with different array configurations but fixed exposure times. The left and middle panels of Fig. 5 show the SNR of the [CII] and [OIII] detections and their line luminosities as a function of the angular resolution⁹ (i.e. ALMA array configuration). Note that the lowest angular-resolution of the [CII] images ($\theta_{\text{beam}} \sim 2''$) is different from that of [OIII] ($\theta_{\text{beam}} \sim 1.2''$) because of the different frequencies of the two FIR lines.

We notice that the SNR and the measured luminosity of the detections decreases at increasing angular resolution. At low angular resolutions, when $\theta_{\text{beam}}/D_{\text{source}} \gtrsim 1.5$ (i.e. $\theta_{\text{beam}} > 1.2''$ for [CII] and $\theta_{\text{beam}} > 0.7''$ for [OIII] observations), both FIR lines are spatially unresolved and have the maximum SNR (~ 10), which is consistent with that returned by the ALMA ETC. The measured line luminosities are consistent with our input values as well.

Moving to higher angular resolutions, the SNR of both FIR lines decreases from 10 to 4. This effect is caused by the surface brightness dimming (SBD) due to the decreasing of the solid angle area, i.e. ALMA beam. We also note that in the same range of angular

⁸ FWHM of the 2D-Gaussian profile

⁹ The angular resolution of ALMA image depends on both the observing frequency (ν_{obs}) and the maximum baselines (b) of the adopted array configurations. The FWHM of the ALMA beam is given by $\theta_{\text{beam}} ['] \approx \frac{76}{b [\text{km}] \nu_{\text{obs}} [\text{GHz}]}$.

resolutions the measured luminosities fall down to $1.5 - 2 \times 10^8 L_{\odot}$, indicating that $\sim 60\% - 70\%$ of the total luminosity is missed in high-angular resolution (and low SNR) observations.

Despite the similar decreasing trend of the two lines, the SNR and line luminosity of the [CII] line drops more rapidly with the angular resolution than the [OIII] line luminosity. The effect of the SBD has indeed a larger impact on the carbon line because the [CII] emission is more extended than the [OIII]. For example, at $\theta_{\text{beam}} = 0.8'' - 1''$ - similar to [CII] size - the [OIII] still appears a point-like source while the [CII] emission is spatially resolved and the line luminosity is underestimated by $20\% - 40\%$.

As most of current ALMA campaigns targeting [OIII] and [CII] in high- z galaxies (Inoue et al. 2016; Carniani et al. 2017; Hashimoto et al. 2019; Harikane et al. 2020; Laporte et al. 2019) have been set to obtain images of both FIR lines with similar angular resolutions, in the right panel of Fig. 5 we report the luminosity line ratio obtained from those synthetic observations having a similar ALMA beam for both lines. At angular resolutions of $\sim 1''$ we infer an average line ratio that is 1.15 times larger than the input value. The different extension of the two lines alters the line ratio estimates, in particular yielding an overestimate of the total [OIII]/[CII] luminosity ratio. At smaller ALMA beams, the ratio estimated from the mock observations is even larger, specifically: 1.35 and 2.1 at $0.6''$ and $0.4''$, respectively. We note that this bias is larger than the typical uncertainty associated to the line ratio estimates (Table 1) and should be taken into account when we investigate intensity of FIR lines in the high- z Universe.

4.2.2 Simulations with different exposure times

So far we have assessed the effect of the SBD on the flux measurements at fixed on-source exposure time, i.e. sensitivity per ALMA beam. Now we take advantage of the second set of simulations to determine the bias driven by sensitivity at different angular resolutions. In Fig. 6 (and Table C1) we report the ratio between the observed and intrinsic flux of our sources as a function of θ_{beam} normalised by [CII] size (D_{source}) and for different SNR, i.e. noise levels.

In synthetic images in which the emission peak is higher than 10σ the measurements are in agreement with the input values, independent of the ALMA array configuration; the discrepancy between the observed flux and the model is lower than 10% , which is of the same order of the noise level and flux calibration uncertainties (i.e. $5\%-10\%$). At lower signal-to-noise ratios ($\text{SNR} < 10$), the discrepancy increases, with the fraction of missed flux depending on the ratio between the angular resolution and the emission extent as well. In particular, at $\text{SNR} = 5$ the flux inferred from the mock observations with the most-compact ALMA array is a factor ~ 0.8 times lower than the input flux, while between 30% and 60% of the flux is missed in the extended configurations.

This second set of simulations catches the effect of SBD on the line luminosity measurement for different SNR and angular resolutions. Once validated against real observation, we can use these results to recover the total FIR line luminosities of high- z galaxies, whose detections have low SNR and are spatially resolved.

4.3 Comparing mock data with observations

In order to verify the results achieved from our simulations, we have searched in the literature for [CII]-emitting galaxies observed multiple times with different ALMA-array configurations, but similar

sensitivity. We have thus found that seven of the ten [CII] emitters reported by Capak et al. (2015) have been recently observed in the ALPINE survey by using a more compact ALMA-array configuration (Le Fèvre et al. 2019; Bethermin et al. 2020). The two datasets, 2012.1.00523.S and 2017.1.00428.L (hereafter C12 and L17), have an angular resolution of $0.7''$ and $1''$, respectively.

Among the seven galaxies in common with the two ALMA programs, we have analysed only three sources, HZ1, HZ3, and HZ4, since the other targets show a multi-component morphology (Carniani et al. 2018a) that would lead to a more complex and ambiguous interpretation with respect to current simulations. The two datasets, data calibration, and analysis are presented in App. D.

Fig. 7 shows the [CII] fluxes of HZ1, HZ3, and HZ4 inferred from the two individual datasets as a function of the θ_{beam} normalised by the extent of [CII] emission (D_{source}) estimated from the observations (see App. D for more details). We notice that the [CII] measurements obtained from L17, which has lower angular resolution, are systematically higher than those estimated in the higher angular-resolution images of C12. This discrepancy is due to the two different ALMA beams. Indeed in the C12 program the angular resolution of the observations is comparable to the [CII] size, so increasing the effect of SBD on the flux measurement. Although the significance of the [CII] detection in C12 is $\text{SNR} > 5$, the sensitivity is not sufficiently high to recover the diffuse and extended emission, whereas in L17 dataset the [CII] line is barely resolved resulting in a higher flux estimate.

In Fig. 7, we also report the predictions from our simulations. For each target we normalise the prediction curve to the weighted mean flux at the average $\theta_{\text{beam}}/D_{\text{source}}$ values of the two datasets. The simulations are fully consistent with the observations, predicting that we miss $20\%-40\%$ of the total flux when the ALMA beam size is similar to the [CII] extension ($\theta_{\text{beam}}/D_{\text{source}} \approx 1$) and the SNR is relative low (< 10). We further note that total flux emission is fully recovered when the ALMA beam is two times larger than the source size. The comparison of the observations and mock data shows that the predictions from our simulations can be used to derive the intrinsic flux of the data when the resolution and sensitivity are not sufficient to retrieve the total emission. In those galaxies where both [CII] and rest-frame UV reveal a multi-component morphology, the correction factor can be applied to each individual component with its relative size. The main limitation of our predictions is that the correction factors suffer from large uncertainty and the total flux cannot be estimated with an error lower than $\sim 20\% - 30\%$. Moreover, our correction factors may not be appropriate for very complicated morphologies. In those cases, ALMA simulations of the target provide a valid alternative to predict the missing flux due to the surface brightness dimming effect.

5 DISCUSSION

In Sec. 3 we find that in our $z = 6 - 9$ sample the extent of [CII] is systematically larger than the [OIII] line. Our findings parallel earlier $z > 4$ galaxy morphological results revealing that [CII] arises from an area typically 2-3 times more extended than the UV-emitting region. In some cases the [CII] emission appear to be extended even up to $6\text{-}10$ kpc, which corresponds to $1''\text{-}1.3''$ at $z \sim 6$ (Carniani et al. 2018a; Matthee et al. 2017, 2019; Fujimoto et al. 2020).

The origin of a such extended [CII] structure is still debated. The diffuse emission can be ascribed to: (a) circumgalactic gas which is illuminated by the strong radiation field produced by the galaxy (Carniani et al. 2017, 2018a; Fujimoto et al. 2020); (b) satellites

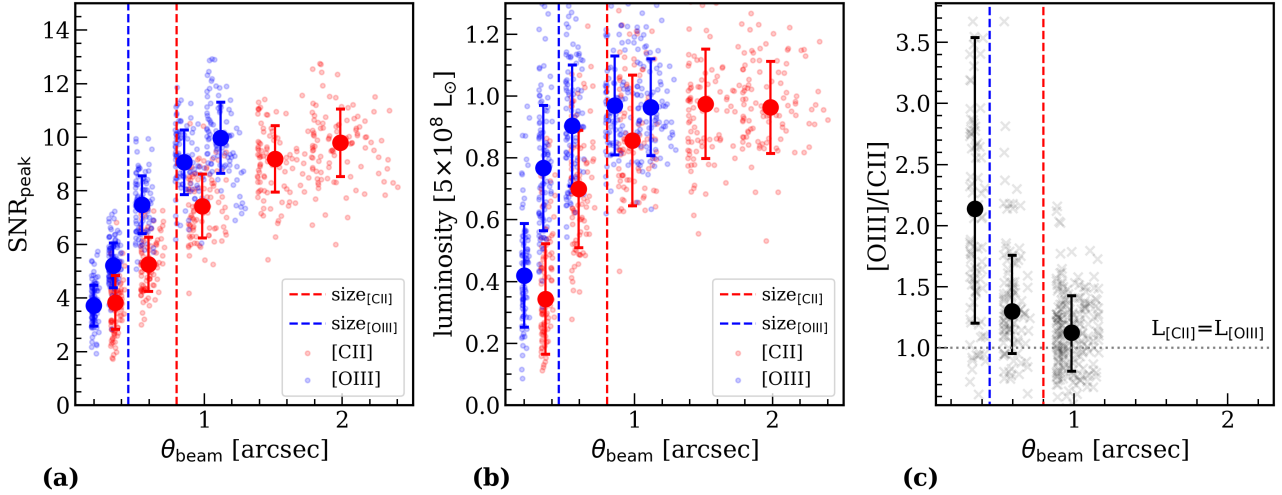


Figure 5. [CII] (red circles) and [OIII] (blue circles) synthetic ALMA observations of $z = 7$ galaxies with $L_{\text{[CII]}} = L_{\text{[OIII]}} = 5 \times 10^8 L_{\odot}$ by using different array configurations, but fixing the exposure times: ($t_{\text{exp}} = 16$ mins for [CII] and $t_{\text{exp}} = 6.5$ h for [OIII]). We have assumed a size for [CII] and [OIII] emission of $0.8''$ and $0.45''$, respectively. Panels (a) and (b) show the signal-to-noise ratio (SNR) of emission peaks and line luminosities, respectively, as a function of angular resolution. Average values for each array configuration are shown with larger marks. In panel (c), we report the [OIII]/[CII] luminosity ratios obtained from [OIII] and [CII] mock observations with similar angular resolutions.

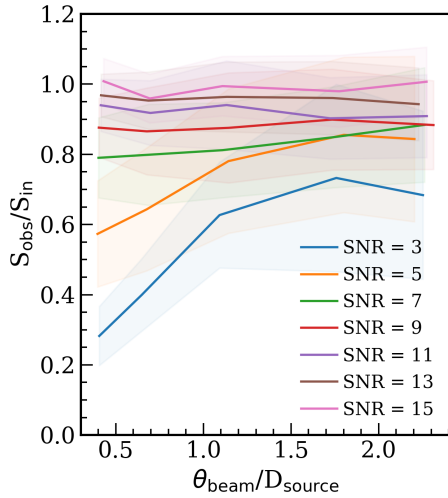


Figure 6. Ratio between measured and intrinsic fluxes, $S_{\text{obs}}/S_{\text{in}}$, as a function of ALMA angular resolution normalised to the [CII] source size, D_{source} , and for different signal-to-noise ratios. The flux is extracted from a region that encompasses the 2σ contour of the emission. If the area of this region is smaller than $2\times$ the ALMA beam, we use a circular region with diameter $1.5\times$ the major-axis of the ALMA beam.

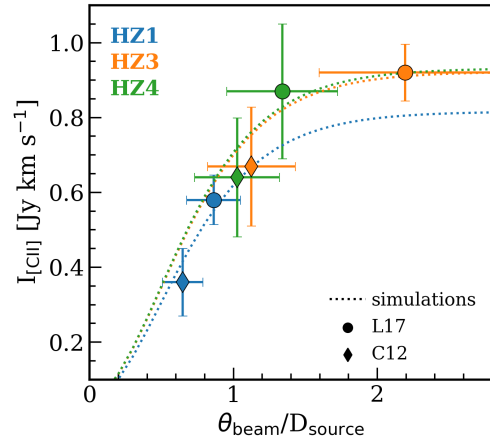


Figure 7. Integrated [CII] flux ($I_{\text{[CII]}}$) vs. ALMA angular resolution (θ_{beam}) normalised to the source size (D_{source}). The measurements of HZ1, HZ3, and HZ4 are indicated with blue, orange, and green marks, respectively. The circles show the estimates obtained from the 2017.1.00428.L dataset (L17; Le Fèvre et al. 2019), while diamond marks indicate the values from the 2012.1.00523.S program (C12; Capak et al. 2015). The predictions from our simulations are represented by the dotted lines.

in the process of accreting (Pallottini et al. 2017a; Carniani et al. 2018b,a; Matthee et al. 2019); (c) outflow remnants, which enriched the circum-galactic medium (Maiolino et al. 2015; Vallini et al. 2015; Gallerani et al. 2018; Fujimoto et al. 2019, 2020; Pizzati et al. 2020; Ginolfi et al. 2020b). Despite its debated origin, it is clear that [CII] is tracing gas on galactic scales different from those of rest-frame UV and [OIII] emission. These different sizes should be taken into account in our measurements.

To date, most of the $z > 6$ ALMA [CII] observations have been carried out with semi-compact array configurations, leading

to $0.5'' < \theta_{\text{beam}} < 1.0''$. Such angular resolutions are sufficient to spatially resolve [CII] emission, and thus reduce the surface brightness within the ALMA beam. Due to this surface brightness dimming effect, ALMA programs might have missed a fraction of diffuse emission resulting into a low [CII] total luminosity. In the following we discuss the effect of the SBD on the $L_{\text{[CII]}}$ -SFR relation and [CII]/[OIII] luminosity ratio estimates.

5.1 [CII] as tracer of SFR in the EOR?

Here we investigate the $L_{\text{[CII]}}$ -SFR relation at $z > 6$ by taking into account the fraction of “missing” [CII] emission on the $L_{\text{[CII]}}$ estimate. In addition to the sample of galaxies discussed in Sec. 3, in this analysis we include all star-forming galaxies at $z > 6$ observed with ALMA so far.

Based on our simulations, we have corrected the observed [CII] luminosities depending on the ALMA beam, SNR of the detection, and extent of [CII] emission. For the upper limits, where the extent of the carbon emission is not known, we assume that the [CII] line is about two times larger than the UV (Carniani et al. 2018a; Fujimoto et al. 2020). We have also derived the total SFR of each source in a uniform way. For those galaxies revealing continuum emission in the ALMA bands, the total SFR has been estimated by adding the SFR_{IR} based on L_{FIR} to the SFR_{UV} calculated from the UV luminosity. We have used a modified blackbody with dust temperature $T_{\text{dust}} = 40$ K and emissivity index $\beta = 1.5$ to reproduce the FIR emission¹⁰ of all galaxies. On the other hand, we have assumed a total $\text{SFR} \approx \text{SFR}_{\text{UV}}$ with no dust correction for those galaxies without continuum detection. Finally, we have taken into account the multi-components morphology of high- z galaxies and performed the proper associations between [CII] and UV components. Top and bottom panels of Fig. 8 show the $L_{\text{[CII]}}$ -SFR diagram before and after applying the correction for the “missing” extended [CII] emission.

After correcting for the SBD effect, the $z > 6$ galaxies become more consistent with the local relation. Most of the upper limits are within the intrinsic dispersion of the relation. Interestingly, the lensed galaxy MS0451-H (Knudsen et al. 2016), which is the only galaxy in the sample with $\text{SFR} < 1 \text{ M}_{\odot} \text{ yr}^{-1}$, still appears to deviate from the local relation by more than 2σ . However, we notice that this source is a lensed arc with an UV extension of $\sim 5 - 6''$, while the ALMA beam is only $1.6''$, hence the flux could be spatially fully resolved (see App. E). Deeper ALMA images of this source are therefore fundamental to recover the total emission and verify if the deviation from the local relation is real or not.

The resulting best fit for the SBD-corrected data is $\log L_{\text{[CII]}} = (1.1 \pm 0.2) \log \text{SFR} + (6.8 \pm 0.2)$ that is consistent within the errors with both the local relation by De Looze et al. (2014) and the $z = 4 - 5$ fitting result reported by Schaerer et al. (2020). We note that our results are in contrast with those shown in the previous study by Harikane et al. (2020) who find a steeper $L_{\text{[CII]}}$ -SFR relation at $z > 6$ (orange curve in Fig. 8). The discrepancy between the two results mainly depends on the handling of [CII] data. Indeed the SBD correction returns more conservative upper limits for $L_{\text{[CII]}}$ and moves most of the [CII] non-detections closer to the local relation. In addition to that, in our sample we have three new [CII] detections that have been considered as non-detections in previous works. Finally, in our study we have uniformly estimate the total SFR of each source based on the UV and FIR luminosity. These three effects explain the difference in normalisation and slope between the best-fit relation of our study and that of Harikane et al. (2020). New [CII] observations of galaxies with $\text{SFR} < 1 - 5 \text{ M}_{\odot} \text{ yr}^{-1}$ will be fundamental to put stronger constrain on the slope of $L_{\text{[CII]}}$ -SFR relation at $z > 6$.

For the nine targets re-analysed in this work we show their location on the $\text{SFR}-L_{\text{[CII]}}$ diagram by adopting both the SFR estimated from the UV+FIR luminosity, or from SED fitting, when available

in the literature. We note that, if we use the SFR estimated from the UV+FIR luminosity (Kennicutt & Evans 2012), which is the same method used for the other [CII] emitters from the literature (e.g. Matthee et al. 2019) and for the ALPINE survey (Schaerer et al. 2020), our sources are in agreement with the local relation, within the uncertainty of 0.48 dex defined by Carniani et al. (2018a). On the other hand, if we adopt the SFR from SED fitting, high- z galaxies appear systematically below the local relation. It is worth mentioning that the SED fitting method returns different SFR estimates with respect to those obtained from UV+FIR calibrators because the assumed star-formation histories, dust-attenuation curves, and stellar population ages are different between the two methods (e.g. Schaerer et al. 2013, 2020; Faisst et al. 2020). In this context, future observations in the near- and mid-IR with JWST (Gardner et al. 2006; Williams et al. 2018; Chevillard et al. 2019), and SPICA (Spinoglio et al. 2017; Egami et al. 2018) will be crucial to better constrain the SED shape and, thus, determine galaxy properties as SFR. In the rest of the work, we use the SFR from UV+FIR luminosity since it is the same method used to determine the local $L_{\text{[CII]}}$ -SFR relation (De Looze et al. 2014).

In Fig. 9 we report the offsets from the local $L_{\text{[CII]}}$ -SFR relation for the $z \gtrsim 6$ galaxies (blue circles) and ALPINE sample (green marks) as a function of redshift before and after correcting for the SBD effect. A linear fit of the total sample gives:

$$\Delta = (-0.13 \pm 0.05)z - (0.54 \pm 0.25) \quad (2)$$

for the uncorrected galaxies (top panel) and

$$\Delta = (-0.05 \pm 0.04)z - (0.20 \pm 0.24) \quad (3)$$

for the corrected sample (bottom panel). The large uncertainties on the best-fit values suggest that there is a no or very weak correlation with the redshift, as also observed at $4 < z < 5.5$ by the ALPINE survey (Schaerer et al. 2020). However the low statistics at $z > 7$ does not allow us to determine definitively whether the $L_{\text{[CII]}}$ -SFR relation evolves with redshift or not.

In conclusion, if we correct for the “missing” [CII] emission and estimate the SFR from UV+FIR luminosity, the whole $z \gtrsim 6$ sample but one seems to be in agreement with the local relation. More specifically the average offset from the local relation is $\Delta_{z=6-9} = -0.07 \pm 0.3$ for the corrected sample and $\Delta_{z=6-9} = -0.2 \pm 0.3$ for the uncorrected one. The small offset indicates that the $z > 6$ targets observed with ALMA so far are not extremely metal-poor galaxies ($Z < 0.2Z_{\odot}$); otherwise, we would expect to observe a clear deviation from $L_{\text{[CII]}}$ -SFR relation as indicated by models and simulations (Vallini et al. 2015; Pallottini et al. 2017a, 2019; Ferrara et al. 2019; Lupi & Bovino 2020).

It is worth stressing that the intrinsic dispersion of the $L_{\text{[CII]}}$ -SFR relation observed at $z > 4$ is 0.42-0.48 dex (Carniani et al. 2018a; Schaerer et al. 2020), two times larger than that inferred from the local HII-like star-forming galaxies (0.28 dex De Looze et al. 2014). Such broad dispersion is indicative of a broader range of ISM properties spanned by such distant galaxies with respect to the local population. In this context, the spatially resolved $\Sigma_{\text{SFR}} - \Sigma_{\text{[CII]}}$ provides a better comparison between high- z and local galaxies, since it is more sensitive to the ISM properties (Ferrara et al. 2019). The [CII] surface brightness at $z > 6$ is systematically lower than that expected from nearby galaxies (see Fig. 10 by Carniani et al. 2018a). This deficit, which is not visible in the integrated $L_{\text{[CII]}}$ -SFR, may indicate that $z > 6$ galaxies deviate from the Kennicutt-Schmidt relation (Pallottini et al. 2019; Ferrara et al. 2019), as recently confirmed in Vallini et al. (2020) for a galaxy at $z = 6.8$ by combining the observations of the [CII] and the rest-frame UV line of CIII].

¹⁰ As the L_{FIR} depends strongly on the assumed T_{dust} and β , we have associated an asymmetric uncertainty of -0.2 dex and +0.4 dex to the L_{FIR} estimates, and thus to the SFR_{IR} and total SFR.

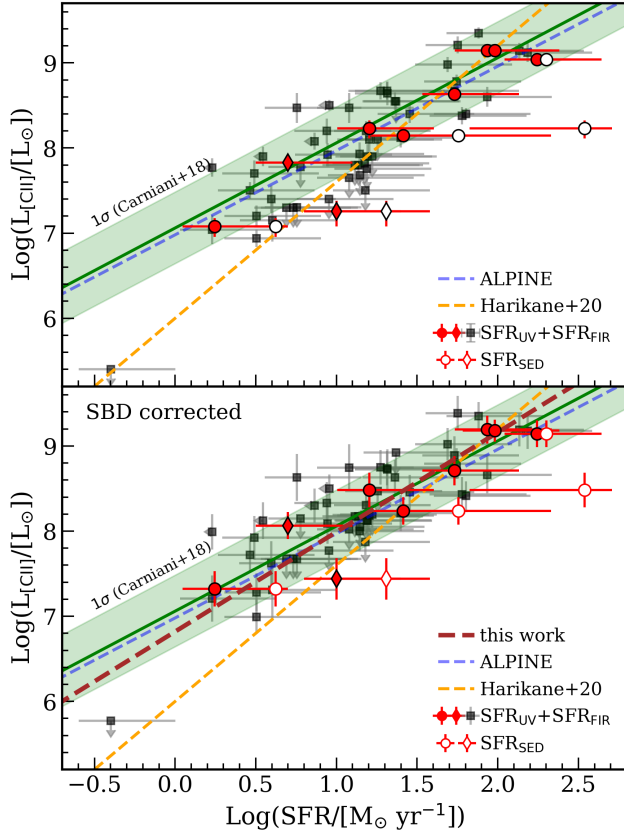


Figure 8. Top and bottom panels show the location of high- z galaxies in the $L_{\text{[CII]}}$ -SFR before and after applying the correction for the SBD effect, respectively. Gray points show the location of all $z \gtrsim 6$ star-forming galaxies reported in the literature so far, including lensed galaxies. Red marks represent the nine galaxies analysed in this work. The empty and filled symbols evidence the difference between the two SFR calibrations based on SED fitting and $L_{\text{UV}}+L_{\text{FIR}}$, respectively, whereas the diamonds distinguish the sources in which the [CII] is not co-spatial with UV emission. The green line shows the local relation by De Looze et al. (2014) for HII-like galaxies ($\log SFR = (1.00 \pm 0.04) \log L_{\text{[CII]}} - (7.06 \pm 0.33)$), with the shaded area corresponding to the 1σ uncertainty for high- z galaxies from Carniani et al. (2018a). The shaded blue line represents the best-fit results from ALPINE survey by Schaerer et al. (2020) ($\log L_{\text{[CII]}} = (0.99 \pm 0.09) \log SFR + (6.98 \pm 0.16)$), while the orange line shows the result from $z > 6$ galaxies by Harikane et al. (2020) ($\log L_{\text{[CII]}} = 1.6 \log SFR + 6.0$). The dashed dark red line in bottom panel illustrates the best-fit results for the SBD-corrected data.

Future ALMA surveys should therefore aim at investigating the spatially resolved relation by performing very deep and high-angular resolution observations.

5.2 [OIII] over [CII] luminosity ratio

Fig. 10 shows the $L_{\text{[OIII]}}/L_{\text{[CII]}}$ ratio as a function of SFR (top panels), and bolometric luminosity defined as $L_{\text{UV}}+L_{\text{FIR}}$ (bottom panels). In the left panels, the line ratios have been estimated directly from the measurements (col. 5 of Table 1), while in the right panels the line luminosities have been corrected for the “missing” extended emission due to the effect of the SBD (col. 6 of Table 1). The correction factors have been determined from our simulations

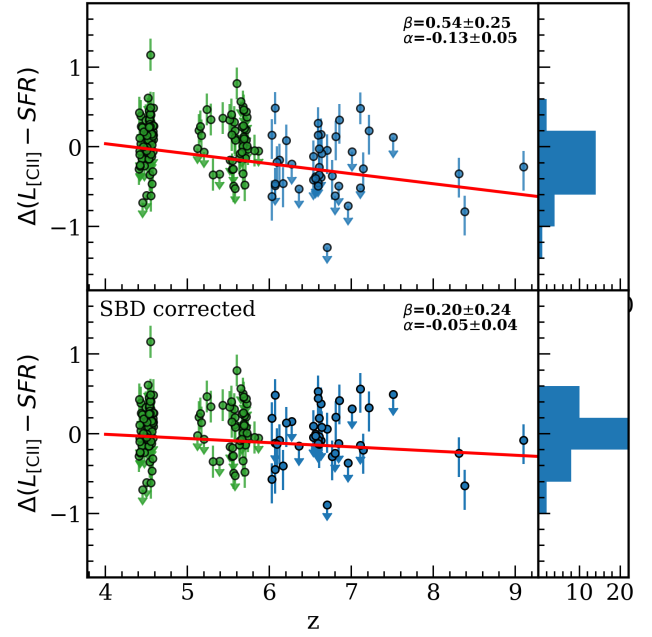


Figure 9. Top and bottom panels show the deviation from the local $L_{\text{[CII]}}$ -SFR relation as a function of redshift before and after applying the correction for the SBD effect, respectively. Blue circles represents $z \gtrsim 6$ star-forming galaxies, while green circles are ALPINE galaxies ($4 < z < 5.5$; Bethermin et al. 2020). Red lines indicate our linear fit and the best-fit parameters are reported in the top-right corner. The top and bottom histograms represent the distributions from $z \gtrsim 6$ sample before and after applying the correction for the SBD effect, respectively.

Table C1), depending on the angular resolution, emission size, and SNR of the detections.

All high- z star-forming galaxies detected both in [OIII] and [CII] exhibit luminosity ratios > 2 , i.e. higher than the average value reported for local metal-rich star-forming galaxies (De Looze et al. 2014; Cormier et al. 2015; Díaz-Santos et al. 2017). However, differently from previous studies, we do not find any value higher than 10. In particular, after the correction for the SBD effect, the luminosity ratios span a range between 1 and 8, that is more consistent with local dwarf galaxies ($1 < L_{\text{[OIII]}}/L_{\text{[CII]}} < 10$; Madden et al. 2013; Cormier et al. 2015) and simulations ($0.5 < L_{\text{[OIII]}}/L_{\text{[CII]}} < 10$; Pallottini et al. 2017b, 2019; Katz et al. 2019; Arata et al. 2020; Lupi et al. 2020).

Fig. 10 also points out the large scatter present in our sample, with no clear dependence of the luminosity ratio on either SFR or $L_{\text{bol}} (= L_{\text{UV}} + L_{\text{IR}})$, in contrast to earlier studies (e.g. Hashimoto et al. 2019; Harikane et al. 2020; Bakx et al. 2020). Indeed the apparent decreasing trend in $L_{\text{[OIII]}}/L_{\text{[CII]}}$ for increasing SFR (and L_{bol}) proposed in previous works (gray dashed line in top panels) was probably driven by extreme (> 10) line ratios quoted in some galaxies with low SFR. However, our re-analysis of ALMA data shows that faint galaxies have a $L_{\text{[OIII]}}/L_{\text{[CII]}}$ similar to the line ratios observed in the whole sample. In addition to that, it is worth mentioning that in Fig. 10 we adopt a uniform approach to estimate the total SFR of each galaxy, which is based on the L_{UV} and L_{IR} , while previous work by Harikane et al. (2020) reports the SFR estimates directly from literature.

As discussed in Harikane et al. (2020), the $L_{\text{[OIII]}}/L_{\text{[CII]}}$ depends mainly on ISM properties such as PDR covering fraction, density,

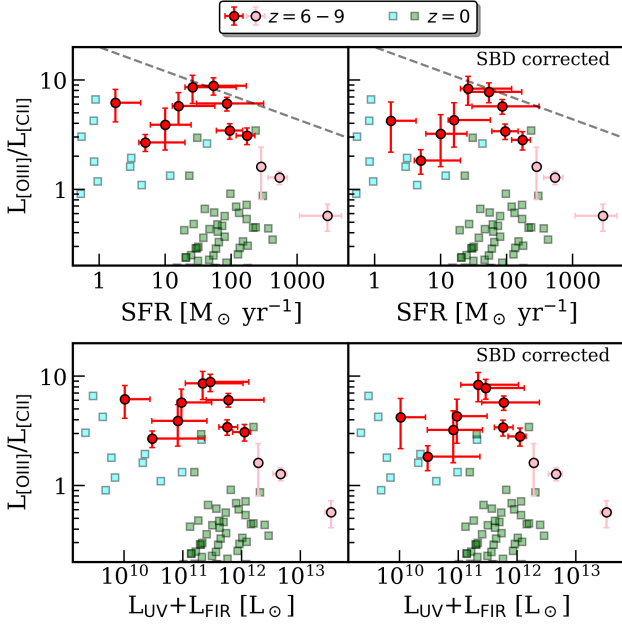


Figure 10. $L_{\text{OIII]}}/L_{\text{CII]}}$ ratio as a function of SFR (top) and $L_{\text{UV}}+L_{\text{FIR}}$ (bottom). In the left and right panels, we show the luminosity line ratio before and after applying the correction for the SBD effect, respectively. Measurements for the nine $z > 6$ star-forming galaxies analysed in this work are shown with red circles. Literature results for $z > 6$ dusty star-forming galaxies (Marrone et al. 2018; Walter et al. 2018) are reported as pink circles. Blue and green squares show the typical ratios observed in local metal-poor and metal-rich star-forming galaxies, respectively (De Looze et al. 2014; Cormier et al. 2015; Díaz-Santos et al. 2017). The grey line represents the best-fitting results for the $z > 6$ galaxies by Harikane et al. (2020).

metallicity, and C/O abundance ratio. Therefore, a weak (or absent) relation with the total SFR is not surprising. However, we expect a dependence with the intensity radiation field as the line ratio intensity should increase with the ionisation parameters (Harikane et al. 2020). Indeed Pallottini et al. (2019) show the $L_{\text{OIII]}}/L_{\text{CII]}}$ ratio reaches values as high as 10 in the central region of their simulated galaxies, where the intensity radiation field has maximum intensity. In the light of these results future deep and high angular-resolution ALMA observations will be fundamental to investigate the spatially resolved $L_{\text{OIII]}}/L_{\text{CII]}}$ ratio in high- z galaxies and compare it with the SFR surface density map.

By using Cloudy calculations, Harikane et al. (2020) find that the $L_{\text{OIII]}}/\text{SFR}$ and $L_{\text{CII]}}/\text{SFR}$ ratios observed in $z > 6$ can be reproduced with PDR covering fractions of 0-10% and ionisation parameters $-2 \lesssim \log U_{\text{ion}} \lesssim -1$, which is 10-100 times higher than what observed in local galaxies. Our new [CII] detections, SBD correction and uniform total SFR calculations for the $z > 6$ galaxies do not change previous results. The new $L_{\text{CII]}}/\text{SFR}$ estimates locate the high- z galaxies in the range $6.4 < \log(L_{\text{CII]}}/\text{SFR}) < 7.4$, that is slightly higher than that reported by Harikane et al. (2020), but $\log U_{\text{ion}} \approx -2$ and a PDR covering fraction of 10% are still requested to reproduce $L_{\text{CII]}}/\text{SFR}$ ratios. As discussed in Harikane et al. (2020) such a low PDR covering fraction implies the presence of escape routes for the Ly α photons and most importantly for the Lyman continuum photons that are responsible of reionization of the Universe. In conclusion such galaxies can play an important role in the reionization process.

6 SUMMARY AND CONCLUSIONS

In the last few years, several ALMA programs have reported weak [CII] emission (or upper limits) for star-forming galaxies at $z > 6$. These low luminosities have suggested that the $L_{\text{CII]}}-\text{SFR}$ relation distant Universe might be different from the local one. Recent ALMA [OIII] observations have also revealed that the $L_{\text{OIII]}}/L_{\text{CII]}}$ line ratio at $z > 6$ is systematically higher than that observed in low- z metal-poor and metal-rich galaxies.

Here we have investigated if the surface brightness dimming (SBD), caused by the combination of the spatial extension of the [CII] emission and the relative high-angular resolution of current ALMA observations, could be the origin of the [CII] deficit reported in earlier works. The main results of our analysis are summarised below.

- We have analysed the ALMA observations of the nine $z = 6-9$ targets observed both in [CII] and [OIII]. By performing different *uv*-tapering to optimise the detection of the diffuse emission, we have identified the [CII] line in the whole sample with a level of significance of $\gtrsim 4\sigma$ at the location and redshift of the either [OIII] or Ly α line. We have found that [CII] emission is systematically $\approx 2\times$ more extended than [OIII] one. This result is in line with other works showing the effective radius of [CII] is in general larger than the radius of UV region by a factor 2-3 (Carniani et al. 2018a; Fujimoto et al. 2020). The origin of such extended component is yet unknown; an appealing explanation is that it may be associated to either inflowing or outflowing material (Maiolino et al. 2015; Carniani et al. 2017, 2018a; Gallerani et al. 2018; Pizzati et al. 2020; Fujimoto et al. 2020; Ginolfi et al. 2020b).

- The extended [CII] emission might lead to a significant underestimation of the total FIR line luminosity in spatially resolved ALMA observations. By performing ALMA simulations with different array configurations and exposure times, we conclude that 20 – 40% of the total [CII] flux might be missed when the angular resolution is comparable to the size of the emitting region, even when the level of significance of the line is $\sim 5-10\sigma$. The fraction of missing flux increases up to 70% when the line is detected with a $\text{SNR} < 5$.

- Using our simulations, further validated against observations, we compute the missing [CII] emission both in our sample and in all galaxies so far observed by ALMA at $z > 6$. We have thus investigated the offset from the local $L_{\text{CII]}}-\text{SFR}$ relation. On average, $z > 6$ galaxies with $\text{SFR} > 5 M_{\odot} \text{ yr}^{-1}$ are located slightly below the local relation ($\Delta z^{6-9} = -0.07 \pm 0.3$), but within the intrinsic dispersion of the relation at high- z . This agrees well with results at $4 < z < 6$ by Schaefer et al. (2020), suggesting little evolution of the $L_{\text{CII]}}-\text{SFR}$ relation with redshift. However we also note that the low statistics at $z > 7-8$ does not allow us to determine definitively whether the relation evolves at very high- z or not.

- We notice that if we adopt the SFR from SED fitting rather than that based on UV+IR luminosity, $z > 6$ star-forming galaxies are systematically offset from the local relation. Therefore future JWST and SPICA observations will be fundamental to put constraints on the SFR, and determine if these galaxies are indeed [CII] faint.

- The new [CII] detections exclude [OIII]/[CII] luminosity ratios > 10 and, once [CII] is corrected for SBD, we find $2 < L_{\text{OIII]}}/L_{\text{CII]}} < 8$, in much better agreement with local dwarf galaxies and simulations. Differently from previous works, we do not confirm a dependence of $L_{\text{OIII]}}/L_{\text{CII]}}$ on SFR and bolometric luminosity, i.e. $L_{\text{UV}}+L_{\text{FIR}}$. As shown by Harikane et al. (2020), we suggest that that $L_{\text{OIII]}}/L_{\text{CII]}}$ is more related to the local properties of the ISM

(e.g. gas metallicity, density, PDR covering fraction) rather than to global galaxy properties.

In summary, the SBD caused by the spatially resolved ALMA observations could have a strong impact on our flux line measurements, and lead to spurious non-detections. The *uv*-tapering is a possible alternative to recover the "missing" extended emission to the detriment of sensitivity. However, this method is not sufficient to infer the total emission arising from the galaxy. Moreover, the missing [CII] emission problem due to the high resolution (and low sensitivity) observations could have an even larger impact in lensed galaxy arcs, since their extension on the sky could be several times the ALMA beam due to gravitational magnification. Lensed galaxies with $\mu > 5 - 10$ may go undetected because the [CII] flux is resolved out, and its surface brightness drops below the detection limit.

Future ALMA programs at low resolutions ($> 1''$) will be ideal to (i) recover the extended [CII] emission component, (ii) investigate both the $L_{\text{[CII]}}$ -SFR relation, and (iii) [OIII]/[CII] luminosity ratio. On the other hand, high-angular resolution ALMA observations with high sensitivity are crucial to study the excitation of the FIR line emission in early galaxy systems, and accurately map the ISM properties in spatially resolved regions.

DATA AVAILABILITY

The data used in the paper are available in the ALMA archive at <https://almascience.nrao.edu>. The derived data and simulations generated in this research will be shared on reasonable request to the corresponding author.

ACKNOWLEDGEMENTS

We thank the anonymous referee for constructive comments and suggestions. This paper makes use of the following ALMA data: ADS/JAO.ALMA#2012.1.00523.S, ADS/JAO.ALMA#2012.A.00040.S, ADS/JAO.ALMA#2012.A.00374.S, ADS/JAO.ALMA#2013.A.00021.S, ADS/JAO.ALMA#2016.1.00856.S, ADS/JAO.ALMA#2017.1.00428.L, ADS/JAO.ALMA#2017.1.00697.S, ADS/JAO.ALMA#2017.A.00026.S. ALMA is a partnership of ESO (representing its member states), NSF (USA) and NINS (Japan), together with NRC (Canada), MOST and ASIAA (Taiwan), and KASI (Republic of Korea), in cooperation with the Republic of Chile. The Joint ALMA Observatory is operated by ESO, AUI/NRAO and NAOJ. AF, SC, and AL acknowledge support from the ERC Advanced Grant INTERSTELLAR H2020/740120. RM acknowledges support from the ERC Advanced Grant 695671 'QUENCH' and from the Science and Technology Facilities Council (STFC). This work reflects only the authors' view and the European Research Commission is not responsible for information it contains. EV acknowledges INAF funding from the program "Interventi aggiuntivi a sostegno della ricerca di main-stream (1.05.01.86.31)".

REFERENCES

- Arata S., Yajima H., Nagamine K., Abe M., Khochfar S., 2020, *MNRAS*, **498**, 5541
- Bakx T. J. L. C., et al., 2020, *MNRAS*, **493**, 4294
- Behrens C., Pallottini A., Ferrara A., Gallerani S., Vallini L., 2018, *MNRAS*, **477**, 552
- Bethermin M., et al., 2020, arXiv e-prints, p. arXiv:2002.00962
- Bradač M., et al., 2017, *ApJ*, **836**, L2
- Capak P. L., et al., 2015, *Nature*, **522**, 455
- Carniani S., et al., 2017, *A&A*, **605**, A42
- Carniani S., et al., 2018a, *MNRAS*, **478**, 1170
- Carniani S., Maiolino R., Smit R., Amorín R., 2018b, *ApJ*, **854**, L7
- Carniani S., et al., 2019, *MNRAS*, **489**, 3939
- Castellano M., et al., 2016, *ApJ*, **818**, L3
- Chevallard J., et al., 2019, *MNRAS*, **483**, 2621
- Cormier D., et al., 2015, *A&A*, **578**, A53
- Dayal P., Ferrara A., 2018, *Phys. Rep.*, **780**, 1
- De Looze I., et al., 2014, *A&A*, **568**, A62
- Díaz-Santos T., et al., 2017, *ApJ*, **846**, 32
- Egami E., et al., 2018, *Publ. Astron. Soc. Australia*, **35**, 48
- Faisst A. L., et al., 2020, *ApJS*, **247**, 61
- Ferrara A., Vallini L., Pallottini A., Gallerani S., Carniani S., Kohandel M., Decataldo D., Behrens C., 2019, *MNRAS*, **489**, 1
- Fujimoto S., et al., 2019, *ApJ*, **887**, 107
- Fujimoto S., et al., 2020, *ApJ*, **900**, 1
- Gaia Collaboration et al., 2016, *A&A*, **595**, A2
- Gallerani S., Pallottini A., Feruglio C., Ferrara A., Maiolino R., Vallini L., Riechers D. A., Pavesi R., 2018, *MNRAS*, **473**, 1909
- Gardner J. P., et al., 2006, *Space Sci. Rev.*, **123**, 485
- Ginolfi M., et al., 2020a, arXiv e-prints, p. arXiv:2004.13737
- Ginolfi M., et al., 2020b, *A&A*, **633**, A90
- Harikane Y., et al., 2020, *ApJ*, **896**, 93
- Hashimoto T., et al., 2018, *Nature*, **557**, 392
- Hashimoto T., et al., 2019, *PASJ*, **71**, 71
- Herrera-Camus R., et al., 2015, *ApJ*, **800**, 1
- Inoue A. K., et al., 2016, *Science*, **352**, 1559
- Jones G. C., Willott C. J., Carilli C. L., Ferrara A., Wang R., Wagg J., 2017, *The Astrophysical Journal*, **845**, 175
- Katz H., Kimm T., Sijacki D., Haehnelt M. G., 2017, *MNRAS*, **468**, 4831
- Katz H., et al., 2019, *MNRAS*, **487**, 5902
- Kennicutt R. C., Evans N. J., 2012, *ARA&A*, **50**, 531
- Knudsen K. K., Richard J., Kneib J.-P., Jauzac M., Clément B., Drouart G., Egami E., Lindroos L., 2016, *MNRAS*, **462**, L6
- Kohandel M., Pallottini A., Ferrara A., Zanella A., Behrens C., Carniani S., Gallerani S., Vallini L., 2019, *MNRAS*, **487**, 3007
- Kroupa P., 2001, *MNRAS*, **322**, 231
- Laporte N., et al., 2017, *ApJ*, **837**, L21
- Laporte N., et al., 2019, *MNRAS*, **487**, L81
- Le Fèvre O., Béthermin M., Faisst A., Capak P., Cassata P., Silverman J. D., Schaerer D., Yan L., 2019, arXiv e-prints, p. arXiv:1910.09517
- Lupi A., Bovino S., 2020, *MNRAS*, **492**, 2818
- Lupi A., Pallottini A., Ferrara A., Bovino S., Carniani S., Vallini L., 2020, *MNRAS*, **496**, 5160
- Madden S. C., et al., 2013, *PASP*, **125**, 600
- Maiolino R., et al., 2015, *MNRAS*, **452**, 54
- Marrone D. P., et al., 2018, *Nature*, **553**, 51
- Matthee J., et al., 2017, *ApJ*, **851**, 145
- Matthee J., et al., 2019, arXiv e-prints,
- McMullin J. P., Waters B., Schiebel D., Young W., Golap K., 2007, in Shaw R. A., Hill F., Bell D. J., eds, *Astronomical Society of the Pacific Conference Series Vol. 376, Astronomical Data Analysis Software and Systems XVI*. p. 127
- Meneghetti M., et al., 2017, *MNRAS*, **472**, 3177
- Olsen K., Greve T. R., Narayanan D., Thompson R., Davé R., Niebla Rios L., Stawinski S., 2017, *ApJ*, **846**, 105
- Ota K., et al., 2014, *ApJ*, **792**, 34
- Ouchi M., et al., 2013, *ApJ*, **778**, 102
- Pallottini A., Ferrara A., Gallerani S., Vallini L., Maiolino R., Salvadori S., 2017a, *MNRAS*, **465**, 2540
- Pallottini A., Ferrara A., Bovino S., Vallini L., Gallerani S., Maiolino R., Salvadori S., 2017b, *MNRAS*, **471**, 4128
- Pallottini A., et al., 2019, *MNRAS*, **487**, 1689

- Pentericci L., et al., 2016, [ApJ](#), 829, L11
- Pizzati E., Ferrara A., Pallottini A., Gallerani S., Vallini L., Decataldo D., Fujimoto S., 2020, [MNRAS](#), 495, 160
- Planck Collaboration et al., 2015, [A&A](#), 580, A22
- Schaerer D., de Barros S., Sklias P., 2013, [A&A](#), 549, A4
- Schaerer D., et al., 2020, arXiv e-prints, p. [arXiv:2002.00979](#)
- Spinoglio L., et al., 2017, [Publ. Astron. Soc. Australia](#), 34, e057
- Sugahara Y., Ouchi M., Harikane Y., Bouché N., Mitchell P. D., Blaizot J., 2019, [ApJ](#), 886, 29
- Tamura Y., et al., 2019, [ApJ](#), 874, 27
- Tazzari M., Beaujean F., Testi L., 2018, [MNRAS](#), 476, 4527
- Vallini L., Gallerani S., Ferrara A., Pallottini A., Yue B., 2015, [ApJ](#), 813, 36
- Vallini L., Ferrara A., Pallottini A., Carniani S., Gallerani S., 2020, [MNRAS](#), 491, 100
- Vanzella E., et al., 2011, [ApJ](#), 730, L35
- Vanzella E., et al., 2017, [ApJ](#), 842, 47
- Vanzella E., et al., 2019, [MNRAS](#), 483, 3618
- Walter F., et al., 2018, [ApJ](#), 869, L22
- Williams C. C., et al., 2018, [ApJS](#), 236, 33
- Zanella A., et al., 2018, [MNRAS](#), 481, 1976
- Zheng W., et al., 2014, [ApJ](#), 795, 93

APPENDIX A: ALMA OBSERVATIONS

In Table A1 we list the properties of ALMA observations and FIR line detections analysed in this work. For some galaxies we report the values from previous works, since our re-analysis returns the same results within the errors.

Table A1. [CII] and [OIII] line properties

	MACS1149-JD1	A2744-YD4	MACSJ0416-Y1	SXDF-NB1006-2	B14-65666	BDF-3329	J0217	J0235	J1211
[CII]									
θ_{beam}	$1.4'' \times 1.3''$	$1.5'' \times 0.9''$	$0.64'' \times 0.46''$	$0.6'' \times 0.5''$	$0.29'' \times 0.23''$	$0.6'' \times 0.5''$	$0.7'' \times 0.7''$	$0.8'' \times 0.7''$	$0.8'' \times 0.6''$
uv -taper	$1.0''$	$0.2''$	$0.27''$	$0.4''$	-	-	-	-	-
SNR_{peak}	3.8	4.7	6.5	4.1	7	5.2	10	8.0	11
$z_{[\text{CII}]}$	9.1099 ± 0.0016	8.3796 ± 0.0002	8.31132 ± 0.00037	7.2127 ± 0.0009	7.1521 ± 0.0004	7.109 ± 0.001	6.2033 ± 0.0009	6.0894 ± 0.0010	6.0291 ± 0.0008
FWHM [km s^{-1}]	130 ± 110	50 ± 16	191 ± 29	230 ± 80	349 ± 31	100 ± 30	316 ± 117	270 ± 135	170 ± 98
$S\Delta v$ [mJy km s^{-1}]	66 ± 18	22 ± 5	120.2 ± 20.4	130 ± 30	870 ± 11	52 ± 7	1.36 ± 0.20	0.42 ± 0.07	1.42 ± 0.15
extent [†]	$1.8'' \pm 1.1''$	$1.6'' \pm 0.9''$	$0.48'' \pm 0.14''$	$1.6'' \pm 0.7''$	$0.85'' \pm 0.11''$	$1.1'' \pm 0.8''$	$1.35'' \pm 0.19''$	$1.0'' \pm 0.3''$	$1.35'' \pm 0.17''$
[OIII]									
θ_{beam}	$0.62'' \times 0.52''$	$0.23'' \times 0.17''$	$0.26'' \times 0.21''$	$0.39'' \times 0.37''$	$0.35'' \times 0.36''$	$0.5'' \times 0.4''$	$0.7'' \times 0.6''$	$0.7'' \times 0.6''$	$0.8'' \times 0.6''$
uv -taper	-	-	$0.35''$	-	-	-	-	-	-
SNR_{peak}	7.4	4.0	6.0	5.2	9	5	12	12	11
z	9.1096 ± 0.0006	8.382 ± 0.001	8.3118 ± 0.0003	7.2120 ± 0.0003	7.1521 ± 0.0004	7.117 ± 0.001	6.2044 ± 0.0013	6.0906 ± 0.0009	6.0295 ± 0.0009
FWHM [km s^{-1}]	154 ± 39	49 ± 4	141 ± 21	80	1.50 ± 0.18	40 ± 10	194 ± 123	389 ± 117	374 ± 162
$S\Delta v$ [mJy km s^{-1}]	49 ± 12	17 ± 10	660 ± 160	450 ± 90	429 ± 37	85 ± 12	4.57 ± 1.06	2.10 ± 0.18	2.69 ± 0.40
extent [†]	$0.8'' \pm 0.3''$	$< 0.2''$	$0.3'' \pm 0.2''$	$0.4'' \pm 0.2''$	$0.66'' \pm 0.09''$	$< 0.4''$	$0.74'' \pm 0.10''$	$0.53'' \pm 0.15''$	$0.74'' \pm 0.17''$

Note. † major axis FWHM size.

APPENDIX B: BLIND-LINE SEARCH METHOD

The blind-line search method used in this work is based on a customised line finder code written in Python and optimised for ALMA observations. The code generates channel maps with different input line widths by averaging the ALMA datacube in frequency. In each channel map the algorithm estimates the noise level and searches for peaks exceeding a fixed SNR threshold, saving their properties (e.g. frequency, position) in a temporary file. Finally the code performs a cross-match between all the extracted candidates to identify duplicates with similar position and frequency, and keeps only the candidates with the highest SNR.

For our study, we have searched candidate lines within 1000 km s⁻¹ from the [OIII] and within 5'' from the UV counterpart. As the [CII] line width is not known a priori, we have used a set of different line widths from 50 km s⁻¹ to 500 km s⁻¹. The SNR threshold of the peaks has been fixed to 3.6 that is the same limit used in the [CII] ALPINE survey (Bethérmin et al. 2020). Finally, we have set a distance of one ALMA beam and $|\Delta\nu| = 500$ km s⁻¹ to discriminate duplicates.

We note that our line finder code is optimised to detect point-source emission. To detect extended emission, we have generated uv -tapered datacubes with different angular resolution for each target and run our customised code on them (Sec. 2).

APPENDIX C: RESULTS FROM ALMA SIMULATIONS

Here we report the results from the simulations with different exposure times and ALMA array configurations. Table C1 shows the ratio between the measured flux density and the input model as a function of signal-to-noise ratio of the detection and the angular resolution normalised by the source size.

APPENDIX D: DATA CALIBRATION AND ANALYSIS OF HZ1, HZ2, AND HZ4

After retrieving the two ALMA datasets, 2012.1.00523.S (Capak et al. 2015) and 2017.1.00428.L (Le Fèvre et al. 2019; Bethérmin et al. 2020), we have reduced the data by adopting the appropriate CASA pipeline version and performed the [CII] flux maps by collapsing the datacubes over a fixed velocity range, depending on the target, for both datasets. In Table D1 we have reported the properties of the ALMA datasets and [CII] images of the three sources.

The two datasets have the same noise level for HZ1 and HZ2, while the sensitivity of the ALPINE data for HZ4 is 2.5 times higher than the rms of the old observations. For HZ4, we have thus split the 2017.1.00428.L, i.e. ALPINE, dataset in six ($\approx 2.5^2$) parts and generated the [CII] datacube from one of the various sub-datasets in order to obtain a final [CII] image with a noise level as high as that of the 2012.1.00523.S program (see Table D1).

By adopting the same prescription used for the mock data (see Sect. 4.1), we have measured the integrated [CII] flux of each galaxy in both datasets. We have also used the `imfit` task in CASA to estimate the deconvolved size of [CII] emission. The integrated flux (Table D1) and source extension estimates are in agreement within the error with those reported by Capak et al. (2015), Bethérmin et al. (2020), and Fujimoto et al. (2020).

APPENDIX E: MS0451-H

MS0451-H is a lensed galaxy at $z = 6.703 \pm 0.001$ with $\text{SFR} = 0.4 M_{\odot} \text{ yr}^{-1}$ and magnification factor $\mu = 100 \pm 20$ (Knudsen et al. 2016). ALMA observations of this galaxy were carried out in Cycle 2 by using a compact array configuration, leading to a natural resolution of $1.6'' \times 0.9''$. The data has been discussed in Knudsen et al. (2016) who reported an upper limit on [CII] luminosity of $3 \times 10^5 L_{\odot}$, i.e. 15 times lower than what expected from the local $L_{\text{[CII]}}$ -SFR relation. By taking into account the intrinsic scatter of the $L_{\text{[CII]}}$ -SFR relation estimated by Carniani et al. (2018a) for the high- z galaxies, $\sigma = 0.48$ dex, the upper limit deviates from the local relation by 2.5σ .

However, the HST/WFC3 F110W image (i.e. rest-frame UV) shows that MS0451-H is a gravitationally lensed arc with an extent of about 5'' (Fig. E1), which is ~ 3 times larger than the ALMA beam. Therefore, the non-detection could be associated to the low surface brightness of the source. We have also re-analysed the ALMA data by performing different uv -tapering in order to recover the extended emission. In the uv -tapered cube with angular resolution of $2.1''$ we have found a potential [CII] line at frequency of 246.783 GHz (Fig. E1, which is consistent with the Ly α redshift ($\Delta\nu = -68$ km s⁻¹) once the intergalactic medium absorption is taken into account (e.g. Maiolino et al. 2015; Pentericci et al. 2016; Matthee et al. 2019). The [CII] emission is offset by 1'' to the East with respect to the UV emission. Since this spatial offset is slightly larger than astrometry accuracy of $0.7''$, we cannot confirm if this potential emission is associate to the arc.

The [CII] emission is detected in the integrated map with an SNR = 4.2 and has an integrated flux density of 42 ± 10 mJy km s⁻¹, which corresponds to $L_{\text{[CII]}} = (4.8 \pm 1.1) \times 10^5 (\mu/100) L_{\odot}$. We note that the error associated with such a large magnification factor might plausibly be higher than 50% when systematics are included (e.g. Meneghetti et al. 2017). Moreover, the vicinity to the critical line also suggests a very steep magnification gradient is present, implying a significant differential magnification can affect the two spatially offset regions.

If we assume that the [CII] emission is as extended as the UV region, our simulations expect that $\sim 60 - 80\%$ of the carbon emission is missed in current ALMA observations. We thus infer a total [CII] luminosity of $L_{\text{[CII]}} = 1.2 - 2.4 \times 10^6 (\mu/100) L_{\odot}$ that is consistent with the local $L_{\text{[CII]}}$ -SFR relation within 1σ . However, deeper ALMA observations are needed to confirm the candidate detection and to estimate the total [CII] emission associated to this lensed galaxy.

This paper has been typeset from a \LaTeX file prepared by the author.

Table C1. Ratio between measured and intrinsic flux as a function of ALMA angular resolution normalised by the [CII] source size ($\theta_{\text{beam}}/D_{\text{source}}$) and signal-to-noise ratio (SNR)

		$\theta_{\text{beam}}/D_{\text{source}}$				
		2.3	1.8	1.1	0.7	0.4
SNR	3	0.68 ± 0.24	0.73 ± 0.27	0.63 ± 0.15	0.40 ± 0.10	0.28 ± 0.08
	5	0.84 ± 0.24	0.86 ± 0.22	0.78 ± 0.21	0.64 ± 0.18	0.57 ± 0.15
	7	0.88 ± 0.16	0.85 ± 0.14	0.81 ± 0.14	0.80 ± 0.14	0.79 ± 0.11
	9	0.88 ± 0.13	0.90 ± 0.14	0.88 ± 0.16	0.87 ± 0.12	0.88 ± 0.08
	11	0.91 ± 0.12	0.90 ± 0.12	0.94 ± 0.13	0.92 ± 0.09	0.94 ± 0.07
	13	0.94 ± 0.10	0.96 ± 0.10	0.96 ± 0.10	0.95 ± 0.08	0.97 ± 0.06
	15	1.01 ± 0.10	0.98 ± 0.10	0.99 ± 0.08	0.96 ± 0.07	1.0 ± 0.06

Table D1. Properties of the ALMA datasets and [CII] images of HZ1, HZ3, and HZ4.

	2017.1.00428.L	2012.1.00523.S
HZ1		
beam	$0.88'' \times 0.80''$	$0.76'' \times 0.52''$
$\sigma_{16}^{(a)}$ [mJy beam $^{-1}$]	0.29	0.31
$I_{[\text{CII}]}$ [Jy km s $^{-1}$]	0.58 ± 0.08	0.36 ± 0.09
$\text{SNR}_{\text{peak}}^{(b)}$	10.3	7.7
HZ3		
beam	$1.32'' \times 0.99''$	$0.76'' \times 0.41''$
$\sigma_{16}^{(a)}$ [mJy beam $^{-1}$]	0.40	0.39
$I_{[\text{CII}]}$ [Jy km s $^{-1}$]	0.92 ± 0.08	0.67 ± 0.15
$\text{SNR}_{\text{peak}}^{(b)}$	16.5	7.3
HZ4		
beam	$0.96'' \times 0.81''$	$0.88'' \times 0.49''$
$\sigma_{16}^{(a)}$ [mJy beam $^{-1}$]	0.24	0.60
	$(0.55)^{(c)}$	
$I_{[\text{CII}]}$ [Jy km s $^{-1}$]	0.89 ± 0.05	0.64 ± 0.16
	$(0.87 \pm 0.18)^{(c)}$	
$\text{SNR}_{\text{peak}}^{(b)}$	18.1	7.2
	$(9.2)^{(c)}$	

Notes: $^{(a)}$ rms measured in a spectral channel of 16 km s $^{-1}$; $^{(b)}$ signal-to-noise ratio of the integrated [CII] map defined as the ratio between the peak and the noise level; $^{(c)}$ rms, integrated flux measured, and SNR from the cropped dataset 2017.1.00428.L of HZ4.

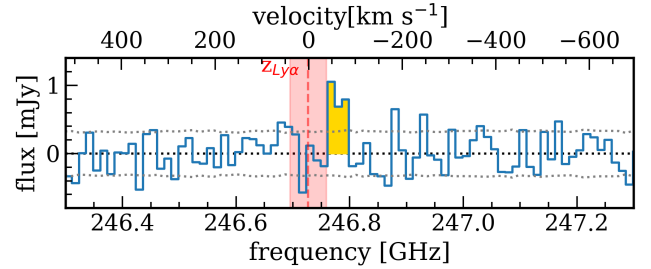
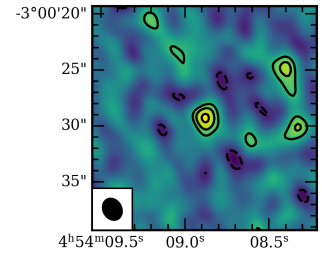
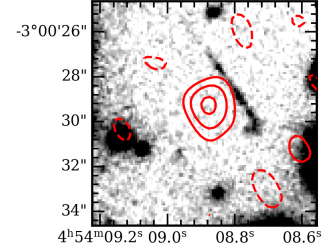


Figure E1. *Top:* HST/WFC3 F110W thumbnail image of MS0451-H arc. Red contours show $\pm 2, 3, 4\sigma$ contours of [CII] emission. *Middle:* uv-tapered [CII] flux map obtained by integrating between -45 km s^{-1} and -95 km s^{-1} with respect to the Ly α redshift (Knudsen et al. 2016). The black lines trace the $\pm 2, 3, 4\sigma$ contours, where 1σ level is 9 mJy km s^{-1} . ALMA beam has been reported in the bottom-left corner. *Bottom:* spectrum of the candidate [CII] detection, with a spectral rebinning of $\sim 16 \text{ km s}^{-1}$. The vertical dashed line shows the redshift inferred from the Ly α , while the grey dotted lines indicate the noise level in the ALMA cube. The gold shaded area represents the frequency range used to obtain the [CII] flux map shown in the middle panel.